Nanoscale

COMMUNICATION

View Article Online
View Journal

Cite this: DOI: 10.1039/d6nr00309e

Received 22nd January 2026,
Accepted 9th April 2026

DOI: 10.1039/d6nr00309e

rsc.li/nanoscale

Iron-induced phase engineering for high color-purity blue LEDs in perovskites

Youngchae Cho,†[a] Sang Wook Park,†[a] Seungmin Baek,†[a] Donghwan Yun,[a] Gwang Yong Shin,[a] Hyeonsu Son,[b,c] Seyeong Song,[d] Hye Won Cho,[e] Hyeseon Shin,[a] Tae Kyung Lee *[b,c] and Gi-Hwan Kim *[a,d,e]

Blue emission in perovskite light-emitting diodes (PeLEDs) remains challenging due to the inherently high bandgap energy. Quasi-two-dimensional (quasi-2D) perovskites have emerged as promising blue PeLEDs, where cascading energy transfer among distinct 2D phases plays a critical role in achieving high device performance. Herein, we propose an additive-assisted phase engineering strategy by incorporating iron additives ($FeBr_3$ and $FeCl_3$) into quasi-2D perovskites. The introduction of iron additives effectively suppresses low-*n* phases and promotes high-*n* phases, enabling bandgap modulation and resulting in a significant narrowing of the photoluminescence full width at half maximum (FWHM). Density functional theory (DFT) calculations reveal that the iron additives thermodynamically stabilize high-*n* phases, accounting for the observed phase redistribution. Blue PeLEDs incorporating $FeCl_3$ achieve an enhanced external quantum efficiency (EQE) of 6.01% and luminance of 227.6 cd m^{-2} compared to pristine devices (3.72%, 177.8 cd m^{-2}). These results suggest that additive-assisted phase engineering provides an effective pathway toward stable, high color-purity blue PeLEDs.

1. Introduction

Metal halide perovskites (MHPs) with the general formula ABX_3 have emerged as versatile optoelectronic materials owing to their unique properties, including tunable bandgaps, high absorption coefficients, and simple solution processability.[1,2] In particular, bandgap tuning across the entire visible spectrum can be achieved by adjusting the composition of halide anions (I^-, Br^-, Cl^-) at the X-site.[3] Perovskite light-emitting diodes (PeLEDs) have attracted increasing attention for display and lighting applications because of their high color-purity arising from the narrow full-width at half maximum (FWHM) of their emission.[4,5] However, blue emission based on chloride-containing perovskites presents significant challenges due to a wide bandgap that leads to unstable energy states and inefficient electron–hole recombination, resulting in low luminous efficiency compared to red and green emissions.[6–8]

To overcome these issues, quasi-two-dimensional (quasi-2D) perovskites have emerged as an effective strategy for stabilizing blue emission.[9] Quasi-2D perovskites are formed by incorporating large organic spacer cations that segment the inorganic $[PbX_6]^{4-}$ framework into discrete layers. This layered configuration confines excitons within the inorganic layers, effectively creating a multiple-quantum-well (MQW) structure.[10–12] The optoelectronic characteristics of quasi-2D perovskites are primarily determined by the distribution of *n* phases, where *n* corresponds to the number of $[PbX_6]^{4-}$ inorganic layers separated by organic spacer cations.[13] In this structure, $n = 1$ represents a single inorganic layer, $n = 2$ indicates two layers, and progressively larger *n* values correspond to thicker inorganic layers with narrower bandgaps and enhanced charge transport properties.[14,15] In typical quasi-2D films, a range of *n* phases coexist, enabling energy funneling from low-*n* phases to high-*n* phases. While this energy transfer process can assist radiative recombination, the coexistence of multiple phases with disparate *n* values can also induce significant energy loss. Moreover, low-*n* phases ($n = 1$–3) exhibit relatively wide bandgaps, and in particular, the $n = 1$ phase is known to promote nonradiative recombination due to strong exciton–phonon coupling.[16–19] Consequently, suppressing low-*n* phases while favoring the formation of high-*n* phases ($n \geq 4$) is essential for achieving efficient and spectrally stable blue emission. Precise modulation

[a]Department of Materials Engineering and Convergence Technology, Gyeongsang National University (GNU), 501 Jinju-daero, Jinju 52828, Republic of Korea. E-mail: choyc0753@naver.com, 2021011461@gnu.ac.kr, yundongwhan@naver.com, gyshin5868@gmail.com, sngmin6505@gmail.com, tjs3371@naver.com, ghkim@gnu.ac.kr
[b]Department of Organic and Nano Engineering, Hanyang University, 222 Wangsimni-ro, Seongdong-gu, Seoul 04763, Republic of Korea. E-mail: shs4663@hanyang.ac.kr, tklee@hanyang.ac.kr
[c]Human-Tech Convergence Program, Hanyang University, 222 Wangsimni-ro, Seongdong-gu, Seoul 04763, Republic of Korea
[d]Research Institute of Molecular Alchemy, Gyeongsang National University (GNU), 501 Jinju-daero, Jinju 52828, Republic of Korea. E-mail: ssy1519@gmail.com
[e]College of Space and Aeronautics, Gyeongsang National University (GNU), 501 Jinju-daero, Jinju 52828, Republic of Korea. E-mail: 250640@gnu.ac.kr
†These authors contributed equally to this work.

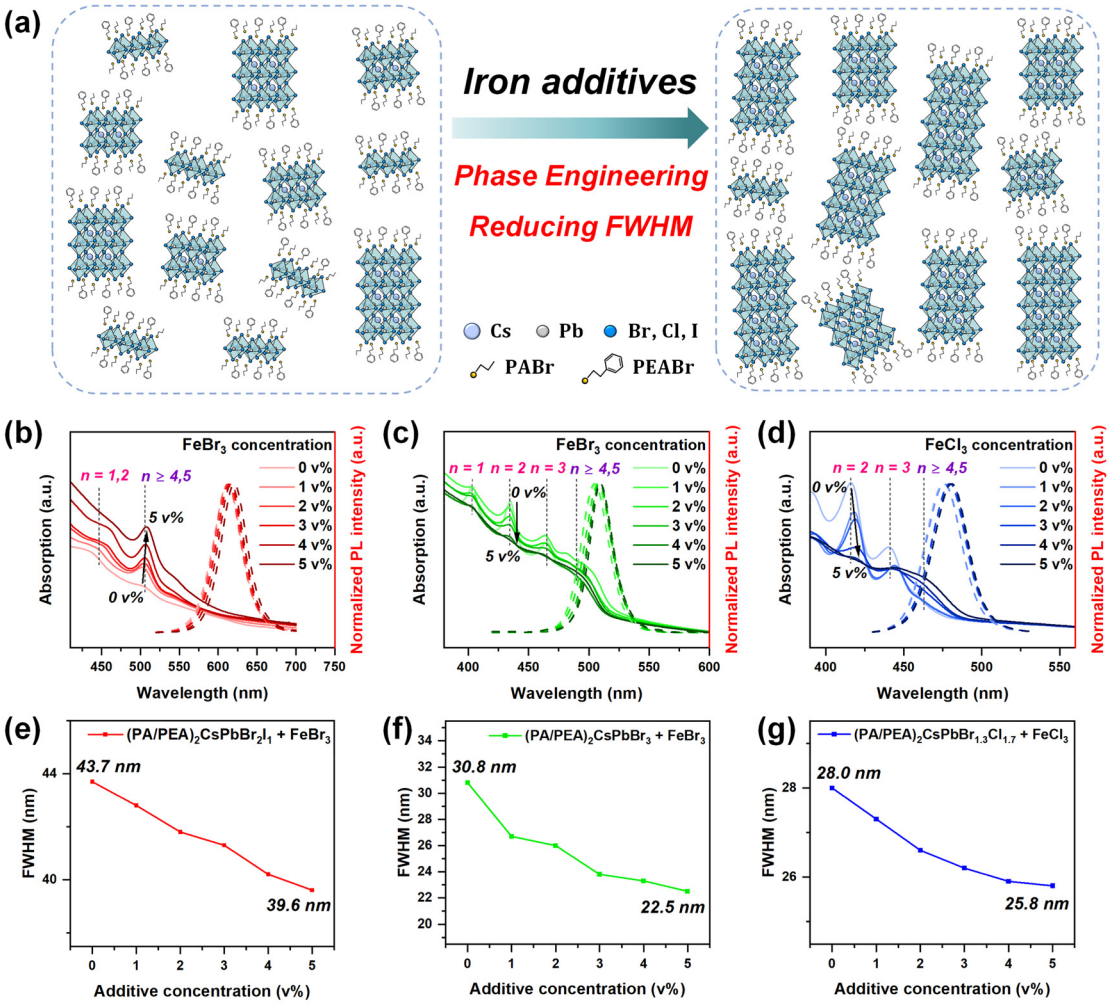

Fig. 1 Optical characteristics of quasi-2D perovskite with iron additives. (a) Schematic illustration of FWHM reduction and phase distribution induced by iron additives incorporation. UV-visible absorption and photoluminescence spectra of (b) $(PA/PEA)_2CsPbBr_2I_1$ with $FeBr_3$, (c) $(PA/PEA)_2CsPbBr_3$ with $FeBr_3$, and (d) $(PA/PEA)_2CsPbBr_{1.3}Cl_{1.7}$ with $FeCl_3$ as a function of iron additive concentration. FWHM changes as a function of iron additive concentration for (e) red emission, (f) green emission, and (g) blue emission.

of the phase distribution has become a key strategy for optimizing quasi-2D PeLEDs efficiency and operational lifetime.[20,21]

Recent studies have demonstrated that introducing specific additives into perovskite precursor solutions can effectively modulate the nucleation and growth processes of perovskite crystals, thereby regulating the phase distribution.[22–24] For instance, Wang *et al.* reported that incorporating YCl_3 creates an internal energy barrier within the crystal lattice, which suppresses nonradiative recombination pathways and enhances luminous efficiency, particularly in blue-emitting PeLEDs.[25] Among various additive strategies, metal halide additives have proven especially effective due to their strong interactions with halide anions in the precursor solution. These interactions modulate the Pb–X bonding and stabilize the perovskite lattice, resulting in effective defect passivation and enhanced optoelectronic performance.[26–29]

In this study, we revealed that the introduction of iron additives ($FeBr_3$ and $FeCl_3$) into quasi-2D perovskites modulates the phase distribution and enhances blue emission performance. The incorporation of Fe^{3+} ions interacts with halide anions in the precursor solution, influencing the bonding environment between the organic and inorganic layers and promoting the dominant formation of high-*n* phases (Fig. 1a). The fundamental mechanisms by which iron additives modify the perovskite phase structure are elucidated through detailed optical characterization and density functional theory (DFT) calculations. Finally, blue PeLEDs incorporating iron additives achieve an external quantum efficiency (EQE) enhancement from 3.72% to 6.01% and an operational stability improvement from 20.7 min to 30.6 min compared to the pristine device.

2. Results and discussion

2.1. Effect of iron additives on red-green-blue emitters

To investigate the intrinsic phase distribution and emission characteristics of quasi-2D perovskite thin films, red, green, and

blue (RGB) emitters were fabricated without the introduction of additives. The precursor solutions were prepared by dissolving precursor powders in dimethyl sulfoxide (DMSO), and the thin films were fabricated using a spin-coating method. Ethyl acetate (EA) was used as an anti-solvent during spin-coating to improve film crystallinity and surface uniformity.[30] The chemical structures employed for the red, green, and blue emitters were $(PA/PEA)_2Cs_{n-1}Pb_n(Br/I)_{3n+1}$, $(PA/PEA)_2Cs_{n-1}Pb_n(Br)_{3n+1}$, and $(PA/PEA)_2Cs_{n-1}Pb_n(Br/Cl)_{3n+1}$, respectively. For simplicity, these compositions are denoted as $(PA/PEA)_2CsPbBr_2I_1$ for red emission, $(PA/PEA)_2CsPbBr_3$ for green emission, and $(PA/PEA)_2CsPbBr_{1.3}Cl_{1.7}$ for blue emission in this study. UV–visible absorption spectroscopy was measured to confirm the formation of multiple n phases within the quasi-2D structures, as shown in Fig. S1a. The red-emitting film showed low-n phase peaks around 430 nm and high-n phase absorption around 510 nm. For the green-emitting film, distinct peaks corresponding to $n = 1$ (400 nm), $n = 2$ (430 nm), $n = 3$ (460 nm), and $n \geq 4$ (480 nm) phases were observed. In the blue-emitting film, absorption peaks corresponding to $n = 1$ (380 nm), $n = 2$ (420 nm), $n = 3$ (440 nm), and $n \geq 4$ (460 nm) were also clearly identified.[31–33] Photoluminescence (PL) analysis revealed distinct emission peaks at 612 nm for red, 506 nm for green, and 475 nm for blue emitter (Fig. S1b).

Recent studies have shown that $FeBr_3$ can stabilize surface ligand in nanocrystal perovskites and $FeCl_3$ can suppress defect states in perovskite solar cells, implying their potential as multifunctional additives in PeLEDs.[34,35] Accordingly, $FeBr_3$ and $FeCl_3$ were introduced into red, green, and blue perovskite solutions, respectively, to modulate the phase distribution and enhance their optoelectronic properties.

The additives were dissolved in DMSO at a concentration of 0.1 mmol and then added to the precursor solutions at various volume ratios of 1, 2, 3, 4, and 5 vol% (v%). The influence of iron additives on the phase distribution and emission characteristics was assessed by UV–visible absorption and PL measurements (Fig. 1b–d). In the red-emitting films, the pristine sample exhibited a low-n phase absorption peak around 430 nm. Upon addition of $FeBr_3$, a noticeable enhancement in the high-n phase absorption between 480 nm and 510 nm was observed, particularly at higher additive concentrations (Fig. 1b). The high-n phase absorption peak was redshifted, which can be attributed to the reduced bandgap as the n phase transitioned toward a dominance of the high-n phases.[36] Correspondingly, the PL emission peak gradually shifted from 612 nm (pristine) to 612 nm, 613 nm, 615 nm, 617 nm, and 621 nm with increasing $FeBr_3$ concentration (Fig. S2a). For the green-emitting films, the introduction of $FeBr_3$ suppressed the low-n phases (n = 1, 2, and 3) and induced a bulk-like absorption profile (Fig. 1c), confirming effective phase engineering. This phase redistribution reduced the bandgap, resulting in a slight redshift in the PL emission from 506 nm to 510 nm across all concentrations (Fig. S2b). Similarly, in the blue-emitting films, the addition of $FeCl_3$ led to a reduction in $n = 1$, $n = 2$, and $n = 3$ phase absorption peaks, while promoting the growth of $n \geq 4$ phase (Fig. 1d).[37,38] The absorption onset continuously redshifted with increasing additive concentration, indicating a decrease in bandgap energy associated with stabilization of high-n phases.[39,40] Correspondingly, the PL emission peak exhibited a redshift from 475 nm (pristine) to 476 nm, 479 nm, 480 nm, 480 nm, and 481 nm with increasing $FeCl_3$ concentration (Fig. S2c). This redshift is attributed to the phase transformation towards bulk-like structures, despite the increased Cl^- content by introducing additives.[41,42] The consistent redshift observed across red, green, and blue systems suggests that bandgap tuning can be achieved through phase engineering, which is closely related to the modulation of the inorganic layer thickness in quasi-2D perovskites.[43]

Moreover, a significant reduction in FWHM was observed across all RGB emitters. The FWHM decreased from 43.7 nm to 39.6 nm for red, from 30.8 nm to 22.5 nm for green, and from 28.0 nm to 25.8 nm for blue (Fig. 1e–g and Table S1). This FWHM narrowing is consistent with improved spectral purity after incorporation of iron additives and with the preferential formation of high-n phases.[44,45]

To further confirm structural changes induced by the additives, X-ray diffraction (XRD) analysis was performed. Typical 3D (bulk) perovskite diffraction peaks corresponding to the (100) and (200) planes were observed near 15° and 30°, respectively (Fig. 2a–c).[46,47] A magnified analysis of the (200) peak revealed that the diffraction intensity increased progressively with higher additive concentrations (Fig. 2d–f).[48] This increase in intensity corroborates the UV–visible absorption results, indicating that the introduction of iron additives promotes the preferential formation of high-n phases within the quasi-2D perovskite films. Notably, for red and blue-emitting perovskites with additive addition, the (200) peak exhibited a shift toward higher diffraction angles with increasing additive concentration (Fig. 2d and f). This shift indicates lattice contraction caused by the substitution of larger halide ions with smaller halide ions introduced *via* $FeBr_3$ and $FeCl_3$, resulting in a more compact crystal structure with reduced lattice parameters.[49] These optical and structural modifications are essential for achieving stable, efficient, and high color-purity light emission, particularly in the blue spectral region.[50,51]

2.2. Density functional theory (DFT) calculations for phase transition

To elucidate the roles of iron additives in the phase distribution, we performed density functional theory (DFT) calculations. Firstly, the analysis of electrostatic potential isosurfaces was conducted to identify the interaction sites between $FeCl_3$/$FeBr_3$ additives and the perovskite precursors (Fig. 3a and Fig. S3). These results suggest that the diverse electron density regions within the iron additive molecules can participate in binding with the precursors, thereby influencing the behavior of the perovskite phase. To further clarify this mechanism, we investigated the influence of iron additives on the perovskite growth. A previous study reported that the $CsPb_2Br_5$ structure was related to the two-dimensional (2D) structure and $CsPbBr_3$ structure was the three-dimensional (3D) struc-

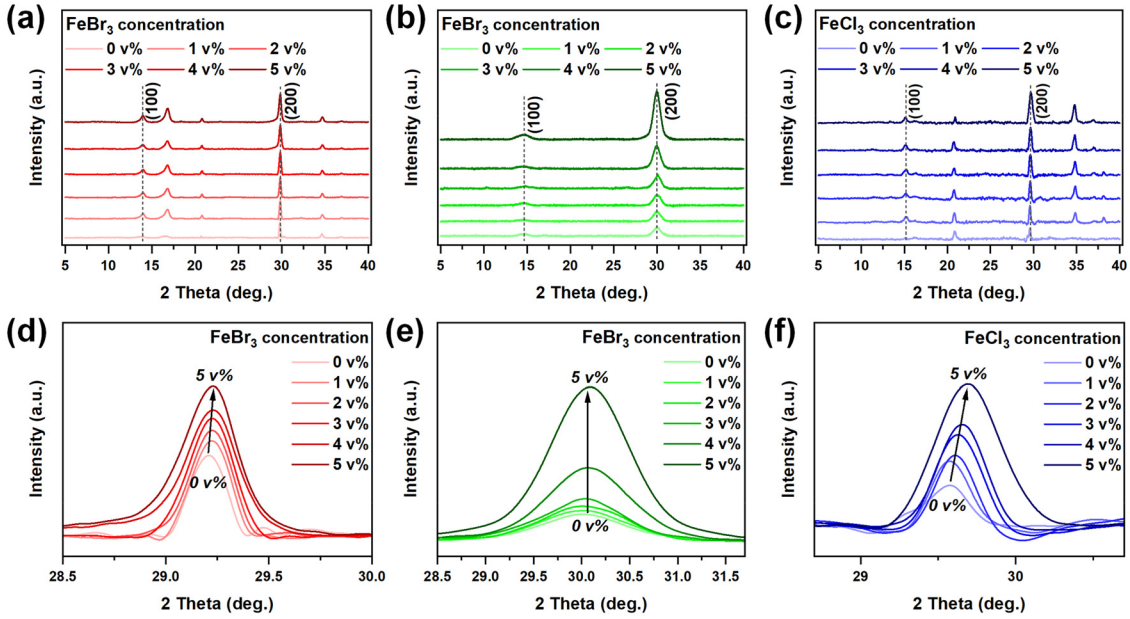

Fig. 2 XRD patterns and the magnified XRD patterns around the (200) peak of (a, d) $(PA/PEA)_2CsPbBr_2I_1$ with $FeBr_3$, (b, e) $(PA/PEA)_2CsPbBr_3$ with $FeBr_3$, and (c, f) $(PA/PEA)_2CsPbBr_{1.3}Cl_{1.7}$ with $FeCl_3$ as a function of iron additive concentration.

ture.[52] Based on this report, we investigated the influence of iron additives on the precursor behavior in the green and blue precursor systems. As a result, the formation of the 3D structure was thermodynamically favored in the presence of iron additives, whereas the formation of the 2D structure was favored in their absence (Fig. 3b and Fig. S4). These results suggest that the additives induce the formation of high-*n* phase perovskite structure. Moreover, we compared the phase stability of the 2D and 3D structures upon the introduction of iron additives (Fig. S5). These results confirmed that the formation of 3D structure induced by iron additives was thermodynamically favorable. Based on calculated results, the structural transitions were suggested in Fig. 3c and Fig. S6, showing the reaction pathway from 2D to 3D induced by iron additives as well as the thermodynamic stability of the 3D phase. Overall, DFT results demonstrate that iron additives promote the phase transition from low-*n* to high-*n* structures through their interactions with the precursors. The additives promote this transition by (1) preferentially stabilizing 3D $PbBr_3$-based structures over 2D Pb_2Br_5-based structures through the favorable interactions, and (2) modulating the precursor chemistry in the solution to shift the thermodynamic equilibrium toward high-*n* phase nucleation and growth. These computational results provide strong theoretical support for our experimental observations of suppressed low-*n* phases, enhanced high-*n* phase content, and improved optoelectronic performance in iron-additive-engineered quasi-2D perovskite films.

2.3. Application to blue PeLEDs with iron additives

Blue emission in PeLEDs requires a large bandgap, which inherently makes electron–hole recombination less efficient compared to red and green emissions. Consequently, the luminous efficiency of blue-emitting devices remains significantly lower than their red and green counterparts.[53–55] Considering that the formation of high-*n* phases can effectively reduce the bandgap, thereby stabilizing blue emission, we introduced iron additives to engineer the phase distribution and improve device performance.[56]

PeLEDs were fabricated using blue perovskite precursor solutions incorporating $FeCl_3$ additives. The device structure consisted of ITO/PEDOT:PSS/Perovskite/TPBi/LiF/Al layers, and the corresponding energy band alignment is illustrated in Fig. 4a. Device performance was evaluated by measuring the current density–voltage–luminance (*J*–*V*–*L*) curves, external quantum efficiency (EQE), and electroluminescence (EL) spectrum. However, devices fabricated with the initial additive concentration (0.1 mmol) exhibited reduced EQE and luminance (Fig. S7 and Table S2). To investigate the reason for this degradation, AFM analysis was performed, revealing an increased RMS roughness, indicative of deteriorated interfacial properties (Fig. S8). Further SEM-EDS analysis of the aggregated regions observed in the AFM images confirmed that excessive additive loading induced precursor aggregation (Fig. S9). Therefore, the additive concentration was reduced to 0.01 mmol, resulting in improved film uniformity. At this optimized concentration, optical characterization still showed a reduction in low-*n* phases and a narrowing of the FWHM, confirming that the phase-engineering effect is preserved (Fig. S10 and Table S3). Subsequently, devices were refabricated using the optimized additive concentration, and their electrical properties were systematically evaluated. Compared with the pristine PeLEDs, devices incorporating $FeCl_3$ additives exhibited a marked enhancement in electronic performance (Fig. S11a, b and Table S4). Introduction of 3 v% $FeCl_3$ exhibited the best

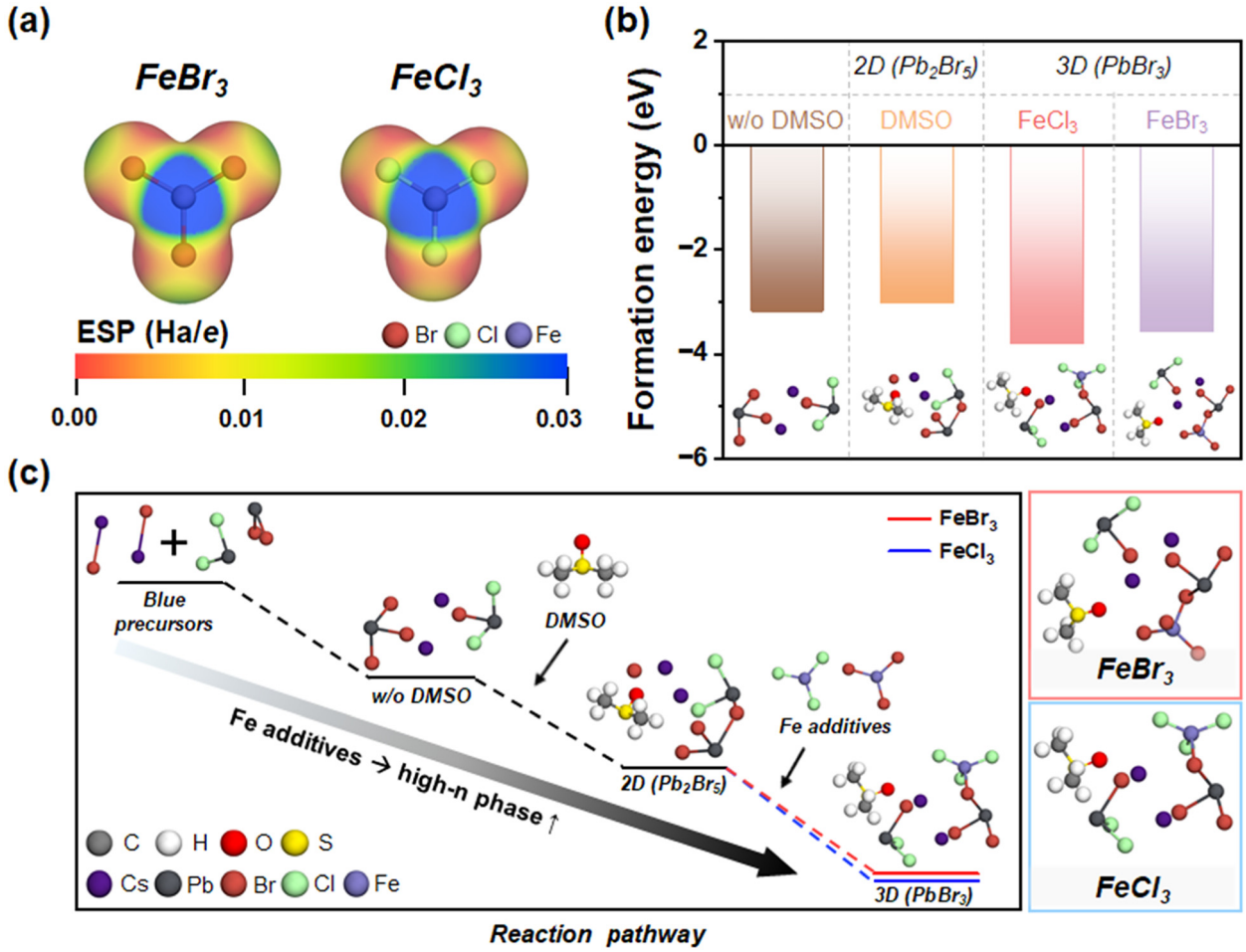

Fig. 3 (a) Electrostatic potential isosurfaces of $FeBr_3$ and $FeCl_3$ molecules. The isosurface value is 0.03 $e/Å^3$. (b) Optimized structures and formation energies of 2D (Pb_2Br_5-based) and 3D ($PbBr_3$-based) structures in the blue perovskite precursor system under different conditions (*i.e.*, w/o DMSO, DMSO, $FeCl_3$, and $FeBr_3$). (c) Schematic reaction pathway of the phase transition from Pb_2Br_5 to $PbBr_3$ in the blue precursor system.

performance, confirming it as the optimal additive concentration. The morphological evolution observed *via* AFM clearly explains this concentration-dependent behavior. The RMS roughness decreased from 2.210 nm (pristine) to 1.510 nm, 1.200 nm, and 1.047 nm for films containing 1, 2, and 3 v% additives, respectively (Fig. S12a–d). However, at 4 and 5 v% concentrations, the RMS roughness increased to 1.737 nm and 2.010 nm, respectively (Fig. S12e and f). This trend suggests that excessive incorporation of the additive beyond 3 v% deteriorates the interfacial morphology, leading to degraded device performance.[57,58] Therefore, the optimized concentration of 3 v% achieves a balance between improved film uniformity and suppressed defect formation, which is critical for enhanced device efficiency. As shown in Fig. 4b and c, the optimized device achieved a maximum luminance increased to 227.6 cd m^{-2} and the EQE improved to 6.01%, compared to 177.8 cd m^{-2} and 3.72% for the pristine device. To verify the reproducibility of the device performance, statistical analysis was performed on 10 devices for each condition, and the corresponding average values and standard deviations are indicated in Fig. S13. This improvement can be attributed to the reduction of leakage current induced by phase engineering.[59] As shown in Fig. S14, the device with 3 v% additive exhibits approximately five times lower leakage current than the pristine device. Consequently, the suppression of low-*n* phases effectively minimizes carrier leakage pathways, leading to reduced nonradiative recombination losses, which contribute to the improved device efficiency.[60]

Electroluminescence (EL) spectra showed that pristine and additive-introduced PeLEDs exhibited emission peaks at 476 nm and 478 nm, respectively (Fig. 4d and Fig. S11c). The redshift in the EL spectrum is consistent with bandgap modulation associated with the suppression of low-*n* phases. The EL FWHM decreases from 23.2 nm to 21.8 nm with increasing additive concentration (Table S5). Additionally, halide migration was examined by tracking the EL peak shift under applied voltages (Fig. S11d–f). The optimized device exhibited minimal halide migration and maintained the EL peak at the maximum EQE.[61]

The operational stability of the LEDs was estimated *via* relative luminance analysis. The T_{50}, defined as the time at which

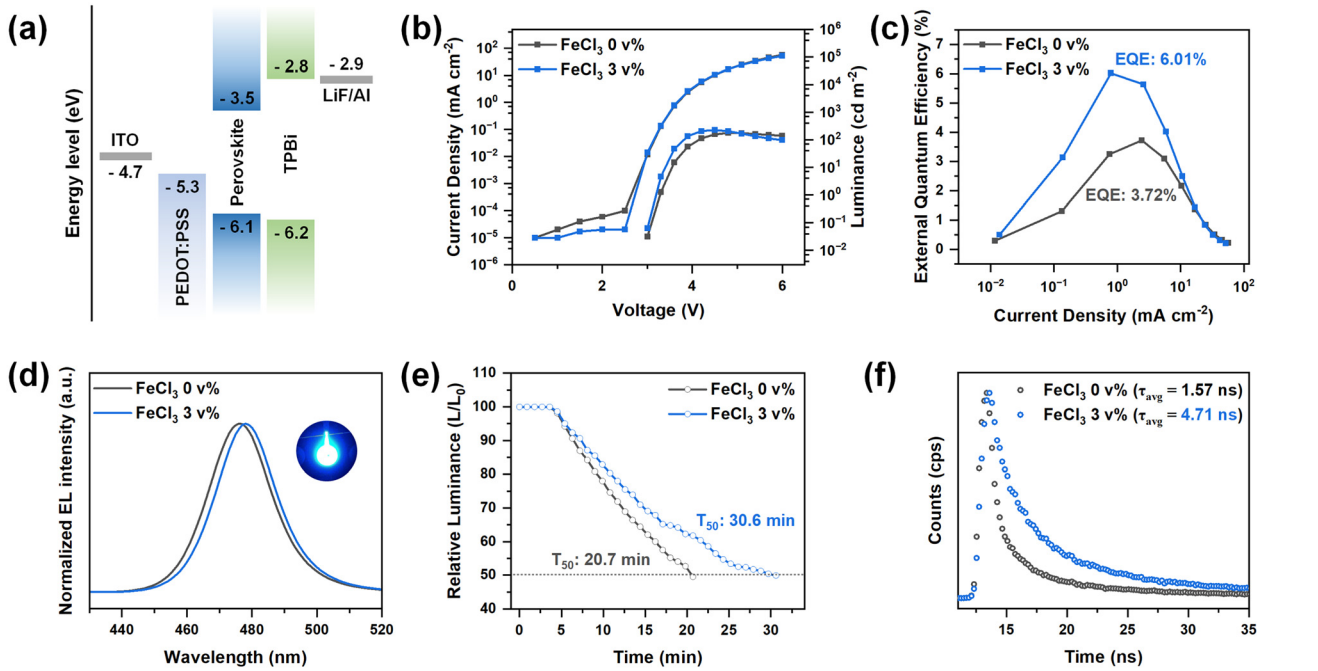

Fig. 4 Characteristics of blue PeLEDs. (a) Energy diagram, (b) *J*–*V*–*L* plot, (c) EQE–*J* curves, (d) electroluminescence spectra (inset shows a photograph of an operating PeLEDs), and (e) operational lifetimes according to relative luminance of PeLEDs. (f) TCSPC spectra of quasi-2D perovskite films.

the luminance decays to 50% of its initial value, was used for comparison.[62] Each device was evaluated under a constant voltage corresponding to the turn-on voltage. The device with 3 v% additives exhibited a T_{50} of 30.6 min, representing a 48% increase over the pristine device (Fig. 4e). This improvement is attributed to the suppression of ion-migration induced by $FeCl_3$ additives, which effectively passivate defects.

To analyze the effect of the additives on perovskite defects and charge transport characteristics, hole-only devices were fabricated. The trap-filled limiting voltage (V_{TFL}) was determined through space-charge-limited current (SCLC) analysis. The V_{TFL} of the pristine device was 1.33 V, while the V_{TFL} of the additive-incorporated device decreased to 1.21 V (Fig. S15a and b). Accordingly, the trap state density (N_{trap}) was calculated using the following equation:

$$N_{trap} = \frac{2V_{TFL}\varepsilon_0\varepsilon_r}{qL^2} \quad (1)$$

where ε_r is the relative permittivity (14.52×10^{-12} F m^{-1}), ε_0 is the vacuum permittivity (8.85×10^{-12} F m^{-1}), q is the elementary charge (1.60×10^{-19} C), and L is the thickness of active layer (30 nm). Consequently, the trap state density decreased from 2.37×10^{18} cm^{-3} for the pristine device to 2.16×10^{18} cm^{-3} for the additive-introduced device. The reduction of V_{TFL} and N_{trap} value indicates that the additives effectively passivate defects, thereby enhancing hole transport.[63]

Time-correlated single photon counting (TCSPC) measurements were performed to evaluate the average carrier lifetime (τ_{avg}) in the perovskite thin films. The pristine film exhibited an average lifetime of 1.57 ns, while the 3 v% $FeCl_3$ film showed an extended lifetime of 4.71 ns, approximately threefold longer (Fig. 4f and Table S6). This substantial increase in carrier lifetime confirms that the introduction of iron additives effectively reduces defect density and suppresses non-radiative recombination pathways, thereby enhancing operational stability.[64,65] Overall, these results demonstrate that the introduction of iron additives effectively contributes to improved device performance in blue PeLEDs.

3. Conclusion

In this study, we demonstrated that stable blue emission can be achieved by introducing iron additives into quasi-2D perovskites. UV-visible absorption and XRD analyses revealed that the incorporation of iron additives effectively suppressed the formation of low-*n* phases while promoting high-*n* phases, leading to a significant narrowing of the photoluminescence FWHM. DFT calculations provided theoretical support for the observed phase redistribution, highlighting the role of iron additives in stabilizing the perovskite crystal structure. As a result of these structural modifications, PeLEDs incorporating iron additives exhibited substantial performance enhancements, achieving approximately 62% higher EQE, 28% higher luminance, and 48% higher operational stability compared to the pristine devices. TCSPC measurements further revealed that the additive-treated films exhibited a threefold increase in average carrier recombination lifetime, thereby suppressing

non-radiative recombination and promoting radiative recombination. Overall, the introduction of iron additives enabled precise control of phase distribution, reduced defect density, enhanced optical properties, and improved device performance. This work provides valuable insight into phase engineering in quasi-2D perovskites through additive incorporation and suggests the potential for developing high color-purity, efficient, and stable blue PeLEDs.

4. Experimental section

4.1. Materials

Cesium bromide (CsBr, 99.999%), cesium iodide (CsI, 99.999%), dimethyl sulfoxide (DMSO, 99.9%), ethyl acetate (EA, ACS reagent, ≥99.5%), iron bromide ($FeBr_3$), iron chloride ($FeCl_3$), and L-phenylalanine (98%) were purchased from Sigma-Aldrich. Phenethylammonium-bromide (PEABr), *N*-propylammonium-bromide (PABr) and phenethylammonium-iodide (PEAI) were purchased from Great Cell Solar Materials. Lead bromide ($PbBr_2$, 98%) purchased from Alfa Aesar. Lead chloride ($PbCl_2$, 98%) and lead iodide (PbI_2, 98%) were purchased from Tokyo Chemical Industry Co. Ltd. Poly(3,4-ethylenedioxythiophene): poly(styrenesulfonate) (PEDOT:PSS) Al 4083 was purchased from Heraeus. 2,2′,2″-(1,3,5-Benzinetriyl)-tris(1-phenyl-1-*H*-benzimidazole) (TPBi) was purchased from Nichem. Aluminum (Al), lithium fluoride (LiF), silver (Ag), and molybdenum trioxide (MoO_3) were purchased from iTASCO.

4.2. Precursor solution preparation

The molar concentration of each precursor solution was prepared following the method described in ref. 66. For the red perovskite film, the precursor solution was prepared by dissolving CsI, $PbBr_2$, PbI_2, and PEAI in DMSO, maintaining a molar ratio of CsI : ($PbBr_2$, PbI_2) : PEAI = 1 : 1 : 1. The halide composition ratio for the red film was Br : I = 2 : 1. For the green perovskite film, CsBr, $PbBr_2$, PEABr, and PABr were dissolved in DMSO with a molar ratio of CsBr : $PbBr_2$: (PEABr, PABr) = 1 : 1 : 1. For the blue perovskite film, CsBr, $PbBr_2$, $PbCl_2$, PEABr, and PABr were dissolved in DMSO, maintaining a molar ratio of CsBr : ($PbBr_2$, $PbCl_2$) : (PEABr, PABr) = 1 : 1 : 1. The halide composition ratio for the blue film was Br : Cl = 1.3 : 1.7. Iron additives ($FeBr_3$, $FeCl_3$) were introduced into each precursor. And a PEDOT:PSS solution was prepared by dissolving 0.89 wt% L-phenylalanine into PEDOT:PSS.

4.3. Preparation of quasi-2D perovskite films

The perovskite precursor solution was filtered using a 0.45 μm pore size polytetrafluoroethylene (PTFE) filter before use. The perovskite films were prepared by spin-coating the precursor solution at 4000 rpm for 60 s, and EA was rapidly poured onto the substrate at 30 s during the spin-coating process. Then, the films were annealed at 60 °C for 20 minutes to remove the residual DMSO.

4.4. PeLEDs fabrication

The patterned ITO substrates were sequentially cleaned in deionized water, acetone, and isopropanol by sonication for 10 min, respectively. After cleaning, the substrates were dried in an oven at 100 °C. Before the spin-coating of PEDOT:PSS, the cleaned substrates were treated with UV-ozone. PEDOT:PSS was coated onto the ITO substrates and annealed at 125 °C for 15 minutes. Subsequently, the perovskite layer was deposited on top of the ITO/PEDOT:PSS films. The films were transferred into a thermal evaporation chamber (3×10^{-6} Torr), and multiple layers of TPBi (40 nm), LiF (1 nm), and Al (100 nm) were sequentially deposited onto perovskite films. The TPBi films were annealed at 85 °C for 5 minutes before the deposition of LiF and Al to improve the interfacial contact between TPBi and the Al electrode. The device structure for SCLC measurements was fabricated ITO/PEDOT:PSS/Perovskite/MoO_3/Ag, ensuring the dominant transport of holes within the active layer by employing a high work function electron blocking layer (MoO_3) and a high work function metal cathode (Ag).

4.5. Perovskite film characterization

UV-visible absorption spectra were measured using a spectrophotometer (Cary 5000, Agilent). Photoluminescence (PL) spectra were measured using a fluorometer (Fluoromax_plus_C, HORIBA) with a xenon lamp as an excitation source. X-ray diffraction (XRD) patterns were obtained using a diffractometer (MiniFlex 6G, Rigaku). Atomic force microscopy (AFM) images were obtained, and RMS values were measured using the MFP-3D Origin, Oxford Instruments. The average lifetime of the perovskite thin films was measured using time-correlated single photon counting (TCSPC), and the samples were evaluated using a 375 nm pulsed laser head (DC-N15-375-6, HORIBA). The surface of the perovskite thin film was coated with gold using a G20 Ion Sputter Coater in preparation for scanning electron microscope (SEM) measurement. And energy-dispersive X-ray spectroscopy (SEM-EDS) analysis was conducted using a scanning electron microscope (SEM AIS 2300C, Korea).

4.6. PeLEDs device characteristics

The current density–voltage–luminance (*J*–*V*–*L*) curve and external quantum efficiency (EQE) characteristics of the LED device were measured using a Keithley 2400 source measurement unit and a spectroradiometer (SR-3AR, TOPCON). The operational stability of the LED device was evaluated using an LED lifetime tester (METRO M600 PLUS, McScience).

4.7. Computational details

All density functional theory (DFT) calculations were conducted using DMol^3 program.[67,68] The Perdew–Burke–Ernzerhof functional within generalized gradient approximation was used for the exchange–correlation energy.[69] Spin polarization calculations were considered and Tkatchenko–Scheffler method was used for dispersion corrections.[70] The self-consistent field tolerance was set to 1×10^{-6} Ha. The geometry optimizations were performed with the convergence cri-

teria of 1×10^{-5} Ha for energy, 0.002 Ha Å^{-1} for force, 0.005 Å for displacement, respectively. The core electrons were treated using all electron relativistic method and double numerical plus polarization basis set (version 4.4) was used. The value of orbital cut-off distance was set to 6.1 Å.

The formation energies of the perovskite phase in each system were calculated using the following equation,

$$\text{Formation } E = E_{\text{product}} - \sum nE_{\text{reactant}}$$

where E_{product} and E_{reactant} are the energy of w/o DMSO, DMSO, $FeCl_3$, and $FeBr_3$ systems and the energy of precursor components (*i.e.*, CsBr, $PbBr_2$, $PbCl_2$, Pb_2Br_5, DMSO, and Fe-based additives) in each system, respectively. n is the number of precursor components in each system.

Author contributions

Youngchae Cho: writing – original draft, methodology, investigation, data curation, visualization. Sang Wook Park: writing – original draft, formal analysis, visualization. Seungmin Baek: methodology, data curation, investigation. Donghwan Yun: investigation. Gwang Yong Shin: investigation. Hyeonsu Son: formal analysis. Seyeong Song: writing – review & editing. Hye Won Cho: writing – review & editing. Hyeseon Shin: investigation. Tae Kyung Lee: writing – review & editing, supervision, funding acquisition. Gi-Hwan Kim: writing – review & editing, supervision, funding acquisition.

Conflicts of interest

There are no conflicts to declare.

Data availability

All data supporting the results of this study are included in the manuscript and its supplementary information (SI). Supplementary information is available. See DOI: https://doi.org/10.1039/d6nr00309e.

Acknowledgements

This research was supported by the National Research Foundation of Korea (NRF) funded by Learning & Academic research institution for Master's PhD students, and Postdocs (LAMP) Program of the National Research Foundation of Korea (NRF) grant funded by the Ministry of Education (No. RS-2023-00301974) and Human Resources Development of the Korea Institute of Energy Technology Evaluation and Planning (KETEP) grant funded by the Ministry of Trade, Industry and Energy of Korea (No. RS-2024-00398425). The computational resource was provided by KISTI (KSC-2023-CRE-0126).

References

1 X.-K. Liu, W. Xu, S. Bai, Y. Jin, J. Wang, R. H. Friend and F. Gao, *Nat. Mater.*, 2021, **20**, 10–21.
2 Y. Fukuda, T. Watanabe, T. Wakimoto, S. Miyaguchi and M. Tsuchida, *Synth. Met.*, 2000, **111**, 1–6.
3 L. Protesescu, S. Yakunin, M. I. Bodnarchuk, F. Krieg, R. Caputo, C. H. Hendon, R. X. Yang, A. Walsh and M. V. Kovalenko, *Nano Lett.*, 2015, **15**, 3692–3696.
4 M. Kim, J. H. Kim, M. Kim, C. S. Kim, J. W. Choi, K. Choi, J. H. Lee, J. Park, Y.-C. Kang and S.-H. Jin, *J. Ind. Eng. Chem.*, 2020, **88**, 84–89.
5 J. Zhang, Z. Ding, X. Liu, Z. He, Y. Chen, S. Cai, J. Wang, G. Li and Y. Liu, *ACS Appl. Mater. Interfaces*, 2024, **16**, 36811–36820.
6 M. Karlsson, J. Qin, K. Niu, X. Luo, J. Rosen, J. Björk, L. Duan, W. Xu and F. Gao, *Front. Optoelectron.*, 2023, **16**, 37.
7 Y. S. Shin, Y. J. Yoon, K. T. Lee, J. Jeong, S. Y. Park, G.-H. Kim and J. Y. Kim, *ACS Appl. Mater. Interfaces*, 2019, **11**, 23401–23409.
8 J. Chae, Q. Dong, J. Huang and A. Centrone, *Nano Lett.*, 2015, **15**, 8114–8121.
9 J. Lu and Z. Wei, *J. Semicond.*, 2020, **41**, 051203.
10 N. Zhou and H. Zhou, *Small Struct.*, 2022, **3**, 2100232.
11 S. Kang, Z. Wang, W. Chen, Z. Zhang, J. Cao, J. Zheng, X. Jiang, J. Xu, J. Yuan and J. Zhu, *Adv. Mater.*, 2025, **37**, 2411027.
12 T. L. Leung, I. Ahmad, A. A. Syed, A. M. C. Ng, J. Popović and A. B. Djurišić, *Commun. Mater.*, 2022, **3**, 63.
13 X. Zhang, R. Munir, Z. Xu, Y. Liu, H. Tsai, W. Nie, J. Li, T. Niu, D. M. Smilgies and M. G. Kanatzidis, *Adv. Mater.*, 2018, **30**, 1707166.
14 Z. Hu, Z. Lin, J. Su, J. Zhang, J. Chang and Y. Hao, *Sol. RRL*, 2019, **3**, 1900304.
15 H. Li, S. Hu, H. Wang, X. Zhang, Y. Tong, H. Qi, P. Guo, G. Zhao, J. Gao and P. Liu, *ACS Appl. Mater. Interfaces*, 2023, **15**, 9574–9583.
16 K. Ma, J. Sun and L. Dou, *Chem. Commun.*, 2024, **60**, 7824–7842.
17 Z.-Q. Ma, Y. Shao, P. K. Wong, X. Shi and H. Pan, *J. Phys. Chem. C*, 2018, **122**, 5844–5853.
18 W. Bi, Q. Cui, P. Jia, X. Huang, Y. Zhong, D. Wu, Y. Tang, S. Shen, Y. Hu and Z. Lou, *ACS Appl. Mater. Interfaces*, 2019, **12**, 1721–1727.
19 F. Li, Y. Li, Z. Yu, X. Du, E. Yang, Y. Ahn, X. Huang, B. R. Lee and S. H. Park, *ACS Mater. Lett.*, 2024, **6**, 1484–1490.
20 P. Chen, Y. Meng, M. Ahmadi, Q. Peng, C. Gao, L. Xu, M. Shao, Z. Xiong and B. Hu, *Nano Energy*, 2018, **50**, 615–622.
21 Y. Chen, S. Yu, Y. Sun and Z. Liang, *J. Phys. Chem. Lett.*, 2018, **9**, 2627–2631.
22 P. Pang, G. Jin, C. Liang, B. Wang, W. Xiang, D. Zhang, J. Xu, W. Hong, Z. Xiao and L. Wang, *ACS Nano*, 2020, **14**, 11420–11430.

23 M. Ma, C. Zhang, Y. Ma, W. Li, Y. Wang, S. Wu, C. Liu and Y. Mai, *Nano-Micro Lett.*, 2025, **17**, 39.
24 M. Abdelsamie, T. Li, F. Babbe, J. Xu, Q. Han, V. Blum, C. M. Sutter-Fella, D. B. Mitzi and M. F. Toney, *ACS Appl. Mater. Interfaces*, 2021, **13**, 13212–13225.
25 Q. Wang, X. Wang, Z. Yang, N. Zhou, Y. Deng, J. Zhao, X. Xiao, P. Rudd, A. Moran and Y. Yan, *Nat. Commun.*, 2019, **10**, 5633.
26 P. Pang, Z. Zhang, B. Wang, T. Sheng and G. Xing, *Nanoscale*, 2025, **17**, 15223–15230.
27 D. Zhang, Y. Fu, C. Liu, C. Zhao, X. Gao, J. Zhang, W. Guo, J. Liu, C. Qin and L. Wang, *Adv. Funct. Mater.*, 2021, **31**, 2103890.
28 K. Yang, J. Mao, J. Zheng, Y. Yu, B. Xu, Q. Zhang, X. Weng, Q. Lin, T. Guo and F. Li, *Adv. Electron. Mater.*, 2023, **9**, 2201199.
29 J. Ye, M. M. Byranvand, C. O. Martínez, R. L. Hoye, M. Saliba and L. Polavarapu, *Angew. Chem.*, 2021, **133**, 21804–21828.
30 J. Liu, N. Li, J. Jia, J. Dong, Z. Qiu, S. Iqbal and B. Cao, *Sol. Energy*, 2019, **181**, 285–292.
31 S. Deng, E. Shi, L. Yuan, L. Jin, L. Dou and L. Huang, *Nat. Commun.*, 2020, **11**, 664.
32 Y. Shang, G. Li, W. Liu and Z. Ning, *Adv. Funct. Mater.*, 2018, **28**, 1801193.
33 Y.-L. Liu, C.-H. Chiang, Y.-C. Chen and M.-L. Tsai, *ACS Sustain. Chem. Eng.*, 2023, **11**, 4580–4587.
34 H. Ding, W. Liu, Y. Zheng, C. Li, H. Jiang and X. Wang, *J. Mater. Chem. C*, 2019, **7**, 1690–1695.
35 B. Gu, Y. Du, S. Fang, X. Chen, X. Li, Q. Xu and H. Lu, *Nanomaterials*, 2022, **12**, 4415.
36 A. Yu, J. Wang, Y. Huo, S. Wang, X. Zhang, T. He, S. Yang, Y. Jiang, L. Zhang and Z. Liu, *Adv. Mater.*, 2025, **37**, 2503704.
37 M. Ezzeldien, S. Al-Qaisi, Z. Alrowaili, M. Alzaid, E. Maskar, A. Es-Smairi, T. V. Vu and D. Rai, *Sci. Rep.*, 2021, **11**, 20622.
38 L. Zhang, C. Sun, T. He, Y. Jiang, J. Wei, Y. Huang and M. Yuan, *Light: Sci. Appl.*, 2021, **10**, 61.
39 M. Ban, Y. Zou, J. P. Rivett, Y. Yang, T. H. Thomas, Y. Tan, T. Song, X. Gao, D. Credgington and F. Deschler, *Nat. Commun.*, 2018, **9**, 3892.
40 N. Chen, Y. Li, S. Lv, Q. Nie, B. Lv, L. Hu and B. Yan, *J. Appl. Phys.*, 2024, **136**, 193105–193115.
41 S. Wang, Z. Chen, G. Zhao and F. Wang, *Comput. Mater. Sci.*, 2023, **230**, 112524.
42 J. S. Manser, J. A. Christians and P. V. Kamat, *Chem. Rev.*, 2016, **116**, 12956–13008.
43 Y.-H. Lee, G. M. Macam, R. A. B. Villaos, L.-Y. Feng, C.-H. Hsu, Z.-Q. Huang, D.-C. Wang, H. Lin and F.-C. Chuang, *J. Phys. Chem. C*, 2024, **128**, 17091–17097.
44 F. Meng, G. Yuan, G. Zhong, L. Qiu, B. Li, G. Sun, Q. Feng, Q. Zeng, Z. Chen and W. Zhu, *Chem. Eng. J.*, 2024, **496**, 154188.
45 Y. Fu, D. Zhang, H. Zhan, C. Zhao, Y. Cheng, C. Qin and L. Wang, *J. Phys. Chem. Lett.*, 2021, **12**, 11645–11651.
46 X. Liu, L. Shi, J. Huang, Z. Liu, P. Zhang, J. S. Yun, A. M. Soufiani, J. Seidel, K. Sun and Z. Hameiri, *Sol. RRL*, 2019, **3**, 1800338.
47 M. Zhou, C. Fei, J. S. Sarmiento and H. Wang, *Sol. RRL*, 2019, **3**, 1800359.
48 M. Alahbakhshi, A. Mishra, G. Verkhogliadov, E. E. Turner, R. Haroldson, A. C. Adams, Q. Gu, J. J. Rack, J. D. Slinker and A. A. Zakhidov, *Adv. Funct. Mater.*, 2023, **33**, 2214315.
49 S. Lee, H. J. Kim, Y. J. Kim, G. W. Yoon, O. Y. Gong, W. B. Kim and H. S. Jung, *Adv. Photonics Res.*, 2024, **5**, 2400039.
50 K. A. Bush, K. Frohna, R. Prasanna, R. E. Beal, T. Leijtens, S. A. Swifter and M. D. McGehee, *ACS Energy Lett.*, 2018, **3**, 428–435.
51 W. Qian, S. Dai, H. Wang, T. Hu, K. Liu, Y. Wang, Q. Guo, X. Yue, Y. Wang and C. Li, *ACS Appl. Mater. Interfaces*, 2025, **17**, 16932–16941.
52 J. Zhu, B. He, X. Yao, H. Chen, Y. Duan, J. Duan and Q. Tang, *Small*, 2022, **18**, 2106323.
53 C. Ge, Q. Fang, H. Lin and H. Hu, *Front. Mater.*, 2021, **8**, 635025.
54 Y. Gao, Q. Cai, Y. He, D. Zhang, Q. Cao, M. Zhu, Z. Ma, B. Zhao, H. He and D. Di, *Sci. Adv.*, 2024, **10**, eado5645.
55 K. Lin, J. Xing, L. N. Quan, F. P. G. de Arquer, X. Gong, J. Lu, L. Xie, W. Zhao, D. Zhang and C. Yan, *Nature*, 2018, **562**, 245–248.
56 M. Worku, Q. He, L.-j. Xu, J. Hong, R. X. Yang, L. Z. Tan and B. Ma, *ACS Appl. Mater. Interfaces*, 2020, **12**, 45056–45063.
57 M.-L. Guo, Y. Lu, X.-Y. Cai, Y. Shen, X.-Y. Qian, H. Ren, Y.-Q. Li, W.-J. Wang and J.-X. Tang, *J. Mater. Chem. C*, 2022, **10**, 2998–3005.
58 Y. Shen, M.-N. Li, Y. Li, F.-M. Xie, H.-Y. Wu, G.-H. Zhang, L. Chen, S.-T. Lee and J.-X. Tang, *ACS Nano*, 2020, **14**, 6107–6116.
59 Y. Chen, Z. He, X. Luo, Z. Liu, S. Cai, J. Zhang, J. Wang, X. Zhai and Y. Liu, *J. Lumin.*, 2025, **282**, 121253.
60 J. Chen, H. Xiang, J. Wang, R. Wang, Y. Li, Q. Shan, X. Xu, Y. Dong, C. Wei and H. Zeng, *ACS Nano*, 2021, **15**, 17150–17174.
61 J.-N. Yang, J.-J. Wang, Y.-C. Yin and H.-B. Yao, *Chem. Soc. Rev.*, 2023, **52**, 5516–5540.
62 Z. Fang, W. Chen, Y. Shi, J. Zhao, S. Chu, J. Zhang and Z. Xiao, *Adv. Funct. Mater.*, 2020, **30**, 1909754.
63 Q. Zhang, D. Zhang, B. Cao, S. Poddar, X. Mo and Z. Fan, *ACS Nano*, 2024, **18**, 8557–8570.
64 Z. Ren, X. Xiao, R. Ma, H. Lin, K. Wang, X. W. Sun and W. C. Choy, *Adv. Funct. Mater.*, 2019, **29**, 1905339.
65 Z. Ren, J. Yu, Z. Qin, J. Wang, J. Sun, C. C. Chan, S. Ding, K. Wang, R. Chen and K. S. Wong, *Adv. Mater.*, 2021, **33**, 2005570.
66 Y. S. Shin, C. B. Park, A. Adhikari, Y. J. Yoon, H. W. Cho, J. G. Son, J. Seo, T. Song, W. Lee and J. Yeop, *ACS Energy Lett.*, 2022, **7**, 3345–3352.
67 B. Delley, *J. Chem. Phys.*, 1990, **92**, 508–517.
68 B. Delley, *J. Chem. Phys.*, 2000, **113**, 7756–7764.
69 J. P. Perdew, K. Burke and M. Ernzerhof, *Phys. Rev. Lett.*, 1996, **77**, 3865.
70 A. Tkatchenko and M. Scheffler, *Phys. Rev. Lett.*, 2009, **102**, 073005.